Contents lists available at ScienceDirect

Engineering Failure Analysis

journal homepage: www.elsevier.com/locate/engfailanal

Fatigue prediction of wind turbine main bearing based on field measurement and three-dimensional elastic drivetrain model

Takeshi Ishihara, Shuai Wang, Yuka Kikuchi *

Department of Civil Engineering, School of Engineering, The University of Tokyo, 7-3-1 Hongo, Bunkyo-ku, 113-8656 Tokyo, Japan

ARTICLE INFO

Keywords:
Wind turbine
Main bearing
Fatigue prediction
Three-dimensional elastic drivetrain model
Life ratio
Load factor

ABSTRACT

Fatigue of main bearing significantly affects the reliability of drivetrain system (DTS) and strongly depends on the DTS configuration. Main bearing failure rate is high for Three-Point Mount wind turbine within the designed life. In this study, a three-dimensional elastic DTS model is established and validated with field measurements. The predicted shaft moments and torque arm motions show good agreements with observations. A numerical pounding model of main bearing is then proposed to evaluate the load factor due to pounding. Finally, the formulas in ISO 281 for predicting main bearing rating life L_{10} are modified by introducing two new parameters: life ratio and load factor. The predicted rating life L_{10} matches well with the onsite records.

1. Introduction

Main bearing is a significant component of the drivetrain system (DTS) in megawatt class wind turbines because its failure causes a relatively long downtime among the DTS components. It is known that the failure rate of the main bearing strongly depends on the DTS configuration [1]. The most common DTS configuration is a three-point mount (TPM), in which the main shaft is supported by an upwind main bearing near the rotor and downwind torque arms at two sides of the gearbox [2]. This configuration is widely used because a single main bearing, a shorter main shaft length, and a lighter bedplate result in smaller nacelle and lower capital cost [3]. However, a survey in the United States indicated that failure rates of TPM main bearings were over 20 % mostly within 6 years [4]. In Tomamae Wind Farm in Japan [5], the failure rate of main bearings in TPM has been reached 65 % within the designed life according to the records. Although the reliability analysis [6,7], fault diagnosis [8,9] and rating lives [10] of main shaft bearings in wind turbines have been widely studied recently, there is still a need to investigate the causes of high failure rates and accurately predict the fatigue life of main bearings.

Dynamic analysis of wind turbine using aeroelastic model is required to assess the fatigue loads on main bearings. The structural and control parameters are unknown and need to be identified from the measurement data as conducted by Yamaguchi et al. [11,12] for an offshore wind turbine. Especially, the wind turbine in Tomamae wind farm was active stall control wind turbine. Active stall control wind turbine occupies about 13 % market share of the global installed capacity [13]. For this type of wind turbine, split pitch control was applied to suppress the divergence of tower vibration due to negative damping [14]. The control parameters of active stall control and split pitch control need to be investigated.

A DTS model is also necessary to evaluate the main bearing fatigue loads. In general wind turbine simulation code FAST [15], the DTS is only modelled with a single degree rotational flexibility, but not bending degrees of freedom. Guntur et al. [16] predicted the

* Corresponding author.
E-mail address: kikuchi@bridge.t.u-tokyo.ac.jp (Y. Kikuchi).

https://doi.org/10.1016/j.engfailanal.2024.108985
Received 27 August 2024; Received in revised form 30 September 2024; Accepted 15 October 2024

main shaft bending moments of a Siemens 2.3 MW TPM wind turbine by using this one-dimensional DTS model and found disagreements with observations due to ignorance of dynamics. In another simulation code Bladed [17], the main shaft can be simulated as a cantilever beam with an additional flexibility in shaft bending dimension, but it cannot describe torque arms behaviors, which are important to the TPM. Hart et al. [18] reviewed that the multibody models are most commonly used for the main bearing modelling due to their speed and relative simplicity. Cardaun et al. [19] evaluated the main bearing loads by the multi body simulation to investigate the impacts of yaw misalignments on the main bearing loads. There, the drive train was modelled as a 2-mass-oscillator with equivalent stiffness and inertia to a gearbox, but the predicted load was not validated with measurements. A suitable DTS model must be proposed for evaluating the fatigue life of the TPM and validated with actual measurements.

The DTS model in multibody system (MBS) was utilized for analyzing the gearbox bearing damages of an MHI 1 MW TPM wind turbine by Shoda et al. [20]. The DTS model in MBS specifically focused on the gearbox but did not pay much attention on the main bearing. Pounding phenomenon was observed at wind turbine main bearings in Tomamae Wind Farm [21], while this phenomenon could not be explained by the DTS model in MBS. In the bearing industry, empirical load factors were applied to machines exposed to pounding and large vibration environments [22]. However, evaluation of pounding for wind turbine main bearing has not been conducted, and a suitable pounding model needs to be introduced. In bridge and building engineering, pounding phenomenon during earthquake were studied for the clearances between bridge girder and tower, between nearby buildings, and between base isolation barriers and buildings [23–26]. Takeda et al. [27] applied a pounding model with finite element method (FEM) by using a pounding spring to calculate the pounding force on the bridge. The pounding model has not been applied to wind turbine main bearings.

The fatigue life of main bearing can be predicted as the fatigue loads on bearings are obtained by a DTS model. For wind turbine bearings, IEC 61400-1 [28] and GL 2010 [29] have the requirements of applying ISO 281 [30] formulas to predict the rating life based on the Lundberg-Palmgren theory [31] for ball and roller bearings as reviewed by Halme and Aderson [32]. Additionally, the life modification factor a_{ISO} is introduced to calculate the modified rating life considering bearing contamination condition. Since the fatigue life of bearings has large fluctuating and theoretically fit with Weibull distribution, the rating life L_{10} with 90 % reliability is defined as a baseline to evaluate fatigue life in consideration of both adequate load capacity and economic sufficiency [30]. However, the formulas in ISO 281 cannot explain the high failure rate of the wind turbine main bearings in Tomamae Wind Farm. This implies that new parameters should be introduced to the formulas in ISO 281.

In this study, fatigue prediction of wind turbine main bearing is conducted based on numerical models and field measurements with considering internal clearances and pounding forces. In section 2, a sophisticated aeroelastic wind turbine model for active stall control wind turbines is proposed to predict the overall wind loads, which are input into the proposed 3D DTS model to evaluate the fatigue loads of the main bearing. A pounding model for main bearing is established to evaluate the pounding forces and load factors. In section 3, the aeroelastic wind turbine and 3D DTS models are validated by field measurements. The predicted main shaft moments and torque arm motions are compared with observations. Bearing operating parameters are determined by on-site survey. The rating life L_{10} of main bearing is predicted considering the new parameters and compared with the onsite records. Finally, the conclusions are summarized in section 4.

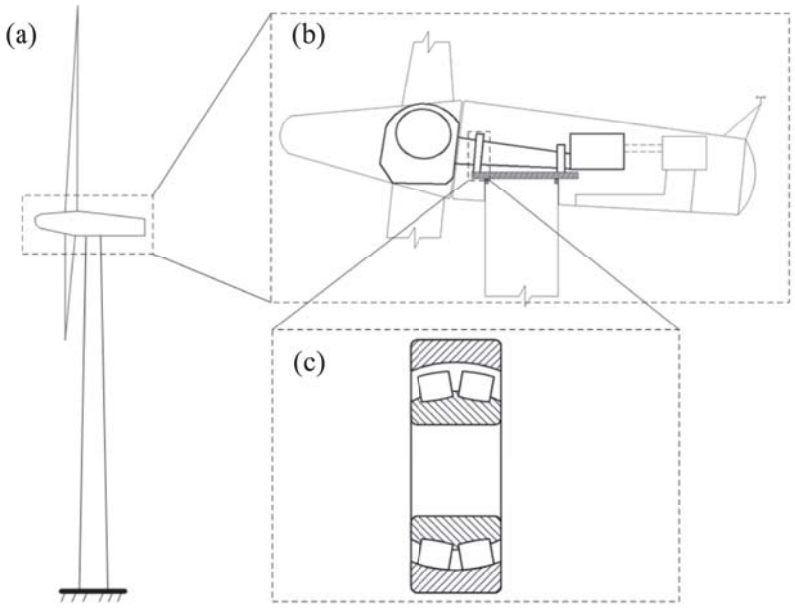

Fig. 1. Numerical models, (a) aeroelastic wind turbine model, (b) 3D DTS model, (c) main bearing model.

2. Numerical models

In section 2, numerical models are described to predict fatigue loads of wind turbine main bearing. Fig. 1 illustrates the schematic of aeroelastic wind turbine model, 3D DTS model, and main bearing model. An aeroelastic wind turbine model is first established to estimate the wind loads on the rotor in section 2.1. A 3D DTS model is then proposed to evaluate fatigue loads on the main bearing in section 2.2. The pounding model for the main bearing is introduced to evaluate the load factor in section 2.3. Finally, the theory of bearing rating life prediction is explained in section 2.4.

2.1. Aeroelastic wind turbine model

An aeroelastic wind turbine model is built up in GH Bladed v4.5 to simulate the wind loads on the rotor. The primary parameters of the target wind turbine are shown in Table 1. Characteristics of tower, nacelle, and rotor are obtained from the manufacturer based on the requirements of IEC 61400–1 [28] and JSCE guideline [33]. The damping ratios of the first and second modes in the flapwise and edgewise directions are set to 1 %. The rotor imbalance is considered with an imbalance mass of 1 %. The tower damping ratio is set to 1 % according to IEC 61400–1. The drag coefficient of tower and nacelle is set to 0.6 and 1.1, respectively, based on the JSCE guideline [33].

The active stall control algorithm for the target wind turbine is employed in the aeroelastic wind turbine model. The split pitch control described in section 3.2 is applied so that the simulated average power is same as the rated one. The time series of wind loads is obtained from the wind turbine model and then converted to main bearing fatigue loads through the DTS model.

The wind speeds are simulated from 4 m/s to 24 m/s with an increment of 2 m/s. Six turbulence seeds generated with Kaimal spectra are adopted to ensure statistical reliability of turbulence simulation. Each seed is 11 min, but the first minute is removed to exclude the uncertainties at initial simulation time steps.

2.2. 3D DTS model

The 1D DTS model is widely used in the current design code, while it cannot accurately evaluate the dynamics of TPM. In this study, a 3D DTS model is proposed as shown in Fig. 2. The main bearing and torque arms are supported by linear and nonlinear springs fixed in X, Y and Z directions above the floor inside the nacelle, while the connection between the main shaft and the gearbox is assumed to be fixed for simplification since the stiffnesses of the main shaft and gearbox are much larger than the stiffnesses of the main bearing and torque arms. The advantage of the proposed 3D DTS model is that it can consider the torque arm displacements in three directions as explained in section 2.2 and can be used to establish the pounding model of main bearing as shown in section 2.3. The rotor, main shaft and gearbox are modelled as lumped masses and moments of inertia at the center of gravities (COGs) as summarized in Table 2. The rotor, main shaft and gearbox are designated by the subscripts r, s and g.

The main bearing and two torque arms of TPM are modelled as elastic elements. The stiffness of main bearing k_{bj} is modelled as linear. The stiffness of torque arms k_{tj} is modelled as nonlinear, representing the rubber bushings as pointed out in a Gearbox Reliability Collaborative Research for TPM wind turbine [34]. Here, the subscript j represents the directions of x, y and z. There exist micrometer scale nonlinearities in the internal clearance and the Hertz contact deformation between the rollers and rings [35]. However, they are small enough and negligible compared to the displacement of the torque arm. The notations of the stiffnesses of the torque arm and main bearing are summarized in Table 3. The stiffnesses of the main bearing and torque arm are identified from the field measurements of main shaft moments and torque arm movements as described in section 3.1. The geometric dimensions of the 3D DTS model are described in Table 4.

In this study, the local DTS model and the global wind turbine aeroelastic model are considered separately since the DTS motion is in millimeter scale, whereas the tower top motions reach meter scale. The wind loads on the rotor predicted by the global wind turbine aeroelastic model are directly applied to the rotor COG of the local DTS model.

The equation of motion for the elastic DTS model can be expressed as Eq. (1) based on the D'Alembert principle. Since the system is nonlinear, a step-by-step Newmark-β numerical method is applied to solve the equation by setting the parameters β and δ to 0.25 and 0.5, respectively.

Table 1
Description of primary parameters of the target wind turbine.

Item	Value	Unit
Manufacturer	Bonus-Energy	–
Type	Upwind	–
Rated power generation	1000/200	kW
Rated rotor speed	21/14	rpm
Rotor diameter	54.2	m
Hub height	45	m
Gearbox	Spur/planetary, 1:69	–
Cut-in/ Cut-out wind speed	3/25	m/s
Wind class	DNV Class B	–

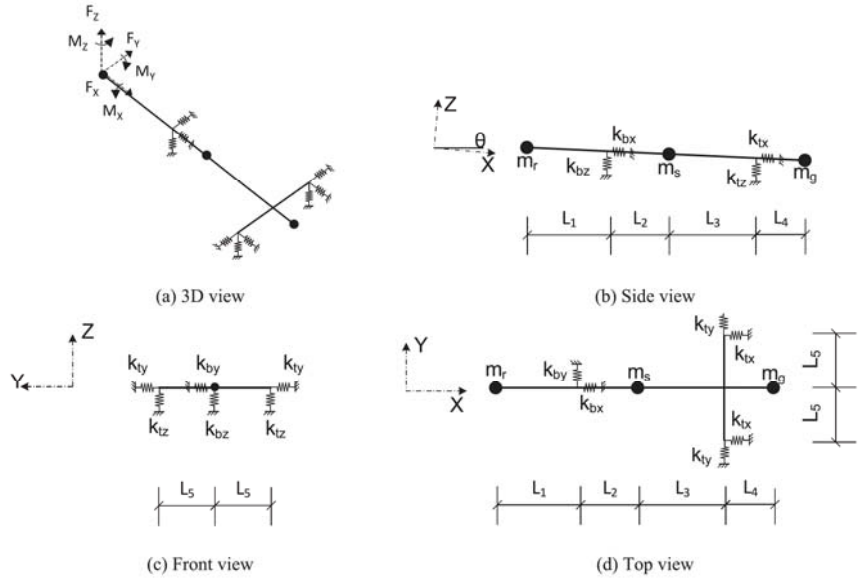

Fig. 2. Three-dimensional elastic DTS model.

Table 2
Summary of lumped masses and moments of inertia of rotor, main shaft and gearbox.

Item	Subscript*i*	Mass	Moment of Inertia		
		m_i[t]	$I_{xx,i}$[kgm^2]	$I_{yy,i}$[kgm^2]	$I_{zz,i}$[kgm^2]
Rotor	r	26	1.2E6	1.4E6	1.4E6
Main shaft	s	5.3	3E2	4.7E3	4.7E3
Gearbox	g	7.5	1.2E4	6.1E3	6.1E3

Table 3
Notations of the stiffnesses of the torque arm and the main bearing of the 3D DTS model.

Notation	Item
k_{bx}	Main bearing stiffness in the X direction
k_{by}	Main bearing stiffness in the Y direction
k_{bz}	Main bearing stiffness in the Z direction
k_{tx}	Torque arm stiffness in the X direction
k_{ty}	Torque arm stiffness in the Y direction
k_{tz}	Torque arm stiffness in the Z direction

Table 4
Geometrical dimensions of the DTS model.

Notation	Item	Value	Unit
L_1	Longitudinal length between rotor COG and main bearing center	1.675	m
L_2	Longitudinal length between main bearing center and main shaft COG	0.498	m
L_3	Longitudinal length between main shaft COG and torque arm center	1.825	m
L_4	Longitudinal length between torque arm center and gearbox COG	0.505	m
L_5	Horizontal length between torque arm center and gearbox COG	0.855	m
θ	Tilt angle	5	degree

$$[M]\{\ddot{u}\} + [C]\{\dot{u}\} + [K]\{u\} = \{F(t)\} - [M]\{\ddot{u}_n\} \tag{1}$$

where $\{u\}, \{\dot{u}\}, \{\ddot{u}\}$ are the displacement, velocity, and acceleration vectors of each node in six degrees of freedom (6 DOF),$\{\ddot{u}_n\}$ is the acceleration vector of the nacelle bedplate, and $\{F(t)\}$ is the wind loads vector. $[M]$, $[C]$, and $[K]$ are the global mass, damping, and stiffness matrixes as shown in Eq. (2).

$$[K] = [T]^T[K_s][T] + [K_b] + [K_t]$$

$$[M] = [T]^T[M_s][T] + [M_l]$$

$$[C] = [M][\Phi][H][\Phi]^T[M]$$

$$[H] = \begin{bmatrix} \ddots & & \\ & 2h_i\omega_i & \\ & & \ddots \end{bmatrix} \tag{2}$$

where $[K_s]$, $[K_b]$ and $[K_t]$ are the local stiffness of shaft beam elements, main bearing spring stiffness, and torque arm spring stiffness, respectively. $[T]$ is the convert matrix. $[M_s]$ and $[M_l]$ are the local mass matrix of shaft beam elements and the lumped mass matrix. $[\Phi]$ is the eigen vector, and $[H]$ is the eigen value matrix with damping ratio of h_i at the corresponding mode i. $[K_s]$, $[M_s]$ and $[T]$ are the same as the matrices for a typical 3D beam element with six degrees of freedom [27].

The local matrices for main bearing stiffness $[K'_{bij}]$ and torque arm stiffness $[K'_{tij}]$ are calculated as in Eq. (3). The locations of $[K'_{bij}]$ and $[K'_{tij}]$ in the global stiffness matrix relate to the end nodes i and j of the spring element. The mass matrix $[M_l]$ consists of the lumped mass and inertia on the corresponding node i. The location of the local lumped mass matrix $[M_i]$ in the global mass matrix is determined by node i as shown in Eq. (4).

$$\left[K'_{bij}\right] = diag\left(k_{bx} \quad k_{by} \quad k_{bz} \quad 0 \quad 0 \quad 0\right), \left[K'_{tij}\right] = diag\left(k_{tx} \quad k_{ty} \quad k_{tz} \quad 0 \quad 0 \quad 0\right)$$

$$[K_b] = \begin{bmatrix} 0 & \cdots & & 0 \\ & \left[K'_{bij}\right] & \cdots & -\left[K'_{bij}\right] & \\ & & \ddots & \vdots & \vdots \\ & sym. & & \left[K'_{bij}\right] & \\ & & & & 0 \end{bmatrix}, \quad [K_t] = \begin{bmatrix} 0 & \cdots & & 0 \\ & \left[K'_{tij}\right] & \cdots & -\left[K'_{tij}\right] & \\ & & \ddots & \vdots & \vdots \\ & sym. & & \left[K'_{tij}\right] & \\ & & & & 0 \end{bmatrix} \tag{3}$$

$$[M_i] = diag\left(m_i \quad m_i \quad m_i \quad I_{xi} \quad I_{yi} \quad I_{zi}\right)$$

$$[M_l] = \begin{bmatrix} 0 & \cdots & & 0 \\ & [M_i] & \cdots & -[M_i] & \\ & & \ddots & \vdots & \vdots \\ & sym. & & [M_i] & \\ & & & & 0 \end{bmatrix} \tag{4}$$

2.3. Pounding model of main bearing

As wear of the main bearing progresses, the internal clearance increases, and the pounding phenomenon begins to occur. In this study, a pounding model of the main bearing is introduced to evaluate the effect of pounding force on fatigue life. The proposed main bearing model is illustrated in Fig. 3 (a). The main shaft and the inner ring are rigidly connected and modelled as a lumped mass. The outer ring and the bearing housing are also rigidly connected, since the stiffness of the bearing housing is usually an order of magnitude larger than that of the roller bearing. The stiffness of roller bearing k_b is set with and without internal clearance, respectively.

The pounding force occurred between the inner ring, outer ring and roller bearings is evaluated using the following equation.

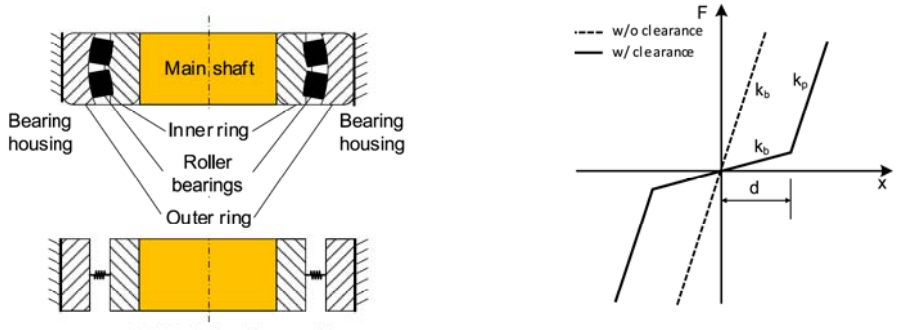

(a) Main bearing model. (b) Force-displacement relationship.

Fig. 3. Pounding model for main bearings.

$$[M]\{\ddot{u}\} + [C]\{\dot{u}\} + [K]\{u\} = \{F_p(t)\} = \{F(t)\} - [M]\{\ddot{u}_n\}$$

$$F_p(t) = \begin{cases} k_p(u+d) & u < -d \\ 0 & -d \le u \le d \\ k_p(u-d) & u > d \end{cases} \tag{5}$$

where $F_p(t)$ is the pounding force, k_p is the pounding stiffness, u is the relative displacement between the inner and outer rings, d is the internal clearance of the roller bearing. If the relative displacement between the inner ring and outer ring is within the clearance, no pounding force occurs. If the relative displacement exceeds the clearance, the pounding force occurs. The force–displacement relationship of pounding model is described in Fig. 3 (b). The notations used in the pounding model are summarized in Table 5. In this study, the pounding effect on the load is modelized as the load factor and the energy loss is considered through the damping ratio in the dynamic analysis.

2.4. Theory of bearing fatigue life prediction

The fatigue life of the main bearing is evaluated by Eq. (6), in which additional parameters, life ratio a_e and load factor f_w, are introduced to take into account the load concentration and the pounding effect on the equivalent dynamic load P'. Those parameters are not considered in the current ISO 281 formula.

$$L_{10} = a_{ISO} a_e \left(\frac{C}{P'}\right)^{\frac{10}{3}}, \quad P' = f_w P \tag{6}$$

where C is the basic dynamic load rating calculated from Eq. (7), P is the dynamic equivalent load of the main bearing calculated from Eq. (8), and the life modification factor a_{ISO} for the material properties and contamination state is calculated from Eq. (9).

ISO 281 defines the basic dynamic load rating of radial roller bearings as:

$$C = b_m f_c (iL_{we}\cos\alpha)^{\frac{7}{9}} Z^{\frac{3}{4}} D_{we}^{\frac{29}{27}} \tag{7}$$

where b_m is the rating factor for currently commonly used high-quality hardened bearing steels confirming to good manufacturing practices and is set to 1.15 for spherical roller bearings (SRB). f_c is a factor that depends on the geometry of the bearing components, the manufacturing precision of the various components, and the materials. f_c is calculated to be 82.8 based on the primary parameters of the main bearing FAG 230/530B summarized in Table 6.

The dynamic equivalent load on the main bearing is calculated as follows:

$$P = XF_r + YF_a$$

$$F_m = \sum_{i=1}^{N} \frac{F_{mi} n_i t_i}{n_e}, \quad n_e = \sum_{i=1}^{N} n_i t_i, \quad m = r, a \tag{8}$$

where F_r and F_a are the radial and axial loads respectively, X, Y are the radial and axial load factors, whose values are determined from Table 7. For wind induced fluctuating loads, the equivalent average bearing load F_m in both radial and axial directions are calculated from the rotational speed and loads in each time step. N is the number of samples, n_i and F_{mi} are the rotational speed and load at operating time t_i.

The life modification factor is calculated as follows:

$$a_{ISO} = 0.1\left[1 - \left(1.5859 - \frac{1.2348}{\kappa^{0.19087}}\right)\left(\frac{e_c C_u}{P}\right)^{0.4}\right]^{-9.185} \tag{9}$$

where κ is the viscosity ratio of the actual kinematic viscosity ν at operating temperature to the reference kinematic viscosity ν_1 at a well-lubricated state, and e_c is the contamination factor. ν is calculated to be 250 mm^2/s for the VG 460 grease considering an operating temperature of about 50 °C and ν_1 is calculated to be 137 mm^2/s. The viscosity ratio κ is evaluated to be 1.82. The contamination factor e_c is determined by Eq. (10) with reference to the contamination categories in ISO 281.

Table 5
Notations used in the pounding model.

Notation	Item
k_b	Roller bearing stiffness
k_p	Pounding stiffness
d	Internal clearance

Table 6
Description of primary parameters of main bearing FAG 230/530B.

Notation	Item	Value	Unit
D	Bearing outside diameter	780	mm
d	Bearing bore diameter	530	mm
B	Bearing width	185	mm
D_{pw}	Pitch diameter of roller set	655	mm
α	Nominal contact angle	8.417	degree
Z	Number of rolling elements per row	30	–
i	Number of rows of rolling elements	2	–
D_{we}	Roller diameter	61.5	mm
L_{we}	Effective roller length	69	mm
C_u	Fatigue load limit	630	kN

Table 7
Values of X and Y for double-row radial roller bearings [30].

	$F_a/F_r \le e$	$F_a/F_r > e$
X	1	0.67
Y	$0.45cot\alpha$	$0.67cot\alpha$
e	$1.5tan\alpha$	$1.5tan\alpha$

$$e_c = a\left(1 - \frac{1.677}{D_{pw}^{1/3}}\right),\ a = 0.0177\kappa^{0.68}D_{pw}^{0.55} \tag{10}$$

The load factor f_w is defined as the ratio of bearing average load with pounding to that without pounding as shown in Eq. (11).

$$f_w = \frac{F'}{F_0} \tag{11}$$

where F_0 and F' are the bearing average loads without and with pounding, respectively, which are evaluated by the pounding model described in section 2.3. In this study, the load factors in the radial and axial directions are assumed to be the same. The equivalent load factor f_{w_equ} is evaluated considering the weights of the wind speed distribution as in Eq. (12).

$$f_{w\_equ} = \sqrt[10/3]{\frac{\sum_i q_i (P_i f_{wi})^{10/3}}{\sum_i q_i (P_i)^{10/3}}} \tag{12}$$

where q_i is the probability, P_i is the equivalent dynamic load, and f_{wi} is the load factor at 10-min average wind speed i.

In addition, the radial internal clearance Δ_r causes the load concentration on specific rollers and rings, resulting in reduced fatigue life [36]. This life reduction must also be applied to wind turbine main shaft bearings, which usually have internal clearances, but is not

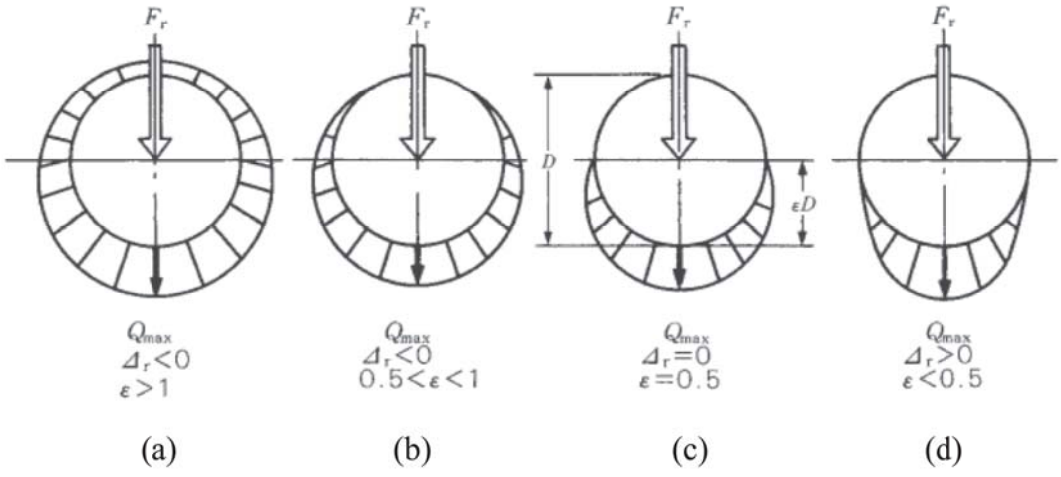

Fig. 4. Radial internal clearance and load distribution.

taken into account in the ISO 281 methodology. The effect of the radial internal clearance on the load distribution around the bearing is illustrated in Fig. 4 as shown in [37]. Here, ε is the factor defined as the ratio of the projected length of the loading area to the raceway diameter when the outer race is partially loaded. When the clearance Δ_r is 0 as shown in Fig. 4 (c), the bearing is loaded by gravity on half the rollers, which is used as the reference value for which the life ratio a_ε is equal to 1. When the clearance Δ_r is positive, the bearing load is concentrated on fewer rollers and the maximum roller load Q_{max} increases, the reduction in life is expressed by a_ε less than 1. When the bearing is preloaded, the clearance Δ_r is slightly less than 0 as shown in Fig. 4 (b), the bearing load is distributed evenly on all rollers, the bearing life is slightly increased. When the clearance Δ_r is more negative as shown in Fig. 4 (a), the bearing life reduces again. When the clearance Δ_r is positive, the bearing load is concentrated on fewer rollers and the life ratio a_ε decreases as the clearance increases as shown in Fig. 4 (d).

To take into account this life reduction due to the effect of the radial internal clearance on the load distribution, the life ratio a_ε is introduced as the ratio of the rating life with internal clearance L_ε to the rating life without internal clearance L and expressed as a function of $f(\varepsilon)$ as shown in Eq. (13):

$$a_\varepsilon = \frac{L_\varepsilon}{L} = F(f(\varepsilon)),\ f(\varepsilon) = \frac{1-2\varepsilon}{\varepsilon} J_r^{-3/4} \tag{13}$$

where J_r is the radial integral, $f(\varepsilon)$ is the intermediate function and is calculated using ε and J_r for spherical roller bearings. Table 8 lists the relationship between ε, J_r and a_ε as look up tables as shown in [37].

$f(\varepsilon)$ is proportional to the radial internal clearance Δ_r and is expressed as Eq. (14) for spherical roller bearings.

$$f(\varepsilon) = \frac{\Delta_r l_{we}^{1/2} \cos\alpha^{7/4}}{0.00018(F_r/iZ)^{3/4}} \tag{14}$$

where i is the number of rows, Z is the number of rolling elements in each row, l_{we} is the effective roller length and α is the nominal contact angle, whose values are shown in Table 6. The radial load F_r is calculated using 1D DTS model considering the gravity and tilt angle of rotor, main shaft and gearbox, whose values are as shown in Table 2 and 4.

The relationship between $f(\varepsilon)$ and Δ_r are then obtained using Eq. (14). Combining with Table 8, The relationship between the life ratio a_ε and clearance Δ_r is obtained and is shown in Fig. 5. When the clearance Δ_r is 0, the life ratio a_ε is 1. When the bearing is preloaded, the clearance is slightly less than 0, the life ratio a_ε is larger than 1 but decreases again as the clearance Δ_r is more negative. On the other hand, when the clearance Δ_r is positive, the bearing load is concentrated on fewer rollers and the life ratio a_ε decreases as the clearance Δ_r increases.

3. Results and discussions

In section 3, field measurements are conducted to validate the numerical models in section 3.1. The wind turbine and DTS models are validated by observations in section 3.2. The parameters regarding contamination and internal clearances are selected based on the investigations of the main bearings. The load factor is calculated using the proposed pounding model. The rating life L_{10} of the main bearing is predicted and validated by field records in section 3.3.

3.1. Description of wind farm and measurement data

In this study, a field measurement campaign is conducted at the Tomamae wind farm in Hokkaido. Wind characteristics are evaluated from Met-Mast observations. The wind farm faces the Japan Sea and is located on an escarpment as shown in Fig. 6. There were 20 wind turbines in the wind farm, and wind turbine No. 3 on the seaside is selected for numerical model validation. Wind

Table 8
Relationship between ε, J_r and a_ε.

ε	J_r	a_ε
0	0	–
0.1	0.1268	0.220
0.2	0.1737	0.469
0.3	0.2055	0.691
0.4	0.2286	0.870
0.5	0.2453	1.000
0.6	0.2568	1.075
0.7	0.2636	1.096
0.8	0.2658	1.065
0.9	0.2628	0.968
1	0.2523	0.805
1.25	0.2078	0.378
1.67	0.1589	0.133
2.5	0.1075	0.029
5	0.0544	0.002

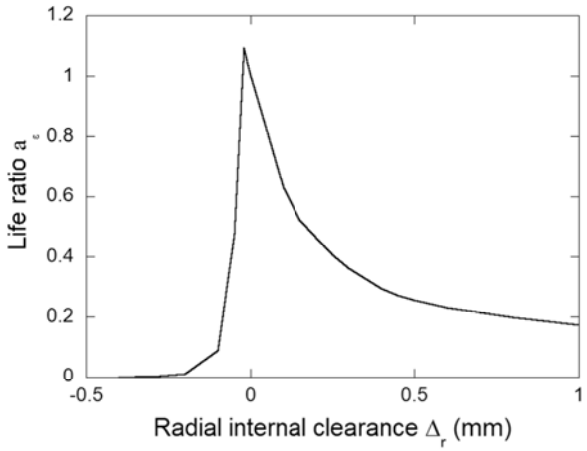

Fig. 5. Relationship between the radial internal clearance Δ_r and the life ratio a_ε.

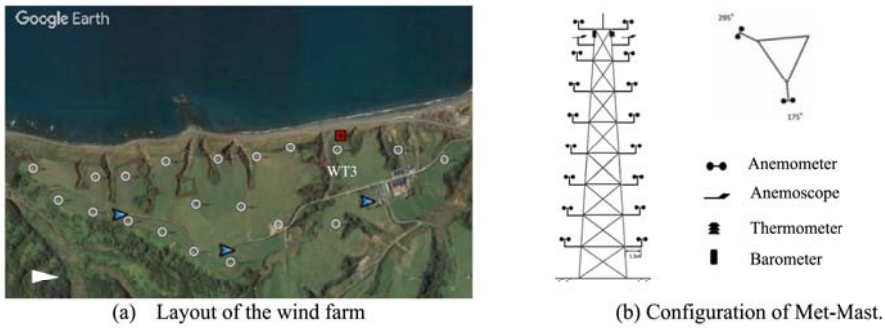

(a) Layout of the wind farm (b) Configuration of Met-Mast.

Fig. 6. Layout of Tomamae wind farm and measurement, where the white open circles denote wind turbines, the red square and the blue triangles indicate the position of LiDAR and Met-masts respectively.

conditions were recorded by Met-Mast for one year starting from November 2015. The measurements of wind turbine and DTS responses were conducted from November 2015 to January 2016.

Annual wind conditions at Tomamae wind farm are obtained from Met-Mast measurement data. Annual average wind speed and wind rose in 16 sectors are obtained as shown in Fig. 7. The relationship between the wind conditions at Met-Mast and the target wind turbine location was studied by Qian and Ishihara [38] using delayed detached eddy simulation. The ratio of average wind speed and turbulence intensity at two locations are obtained, and the wind condition is converted from Met-Mast to the target wind turbine. The ratio of the wind speed and turbulence intensity is close to 1, which means there is little difference in the wind condition at the two

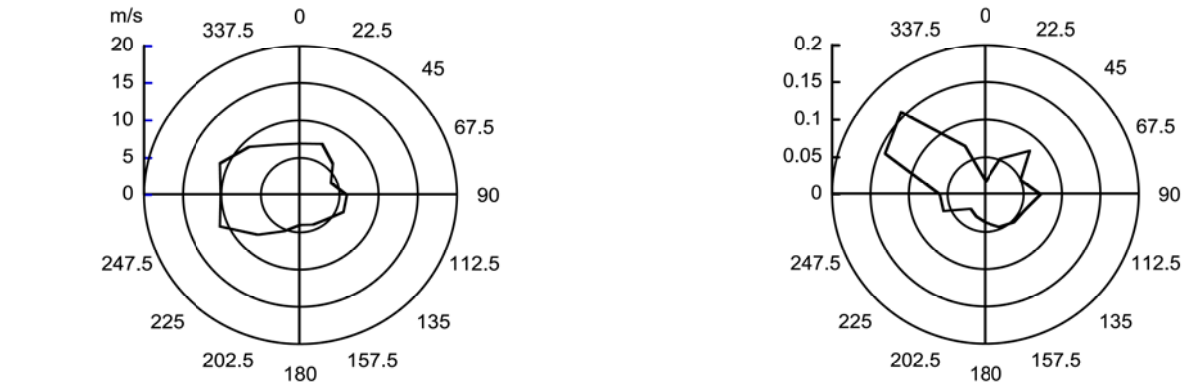

(a) Annual mean wind speed in each wind direction (b) Wind rose

Fig. 7. Distribution of wind speed and wind rose converted from Met-Mast to wind turbine location.

locations.

Wind shears with exponents α of 0.07 and 0.25 are observed at the sea side and the land side, respectively. The mean wind shear calculated by considering the probability of wind direction is 0.15. A Rayleigh distribution with an annual wind speed of 7.7 m/s is used and is shown in Fig. 8 (a). IEC 61400–1 requires the 90 % quantile of the turbulence intensity in the normal turbulence model (NTM) for the evaluation of fatigue loads [28]. As depicted in Fig. 8 (b), the NTM of Class A is close to the observed 90 % quantile. The relationship between longitudinal turbulence and the mean wind speed is calculated by Eq. (15).

$$\sigma_1 = I_{ref}(0.75V_{hub} + b) \tag{15}$$

where V_{hub} is the mean wind speed at hub height, σ_1 is the longitudinal turbulence at wind speed V_{hub}, I_{ref} is set to 0.16, and b is 5.6. The lateral turbulence σ_2 and the upward turbulence σ_3 are set to 0.8 σ_1 and 0.5 σ_1, respectively.

The dynamic responses of the No.3 wind turbine are measured to validate the aeroelastic wind turbine model. Eight strain gauges are installed on the tower shell to measure the vertical strain at a height of 3.82 m as Fig. 9. The initial offset of the strain gauges is calibrated using the measured strain data during a nacelle rotation test in which the nacelle yaw angle is rotated 360 when the wind turbine is in the parked condition [11]. The tower bending moments are converted from the observed strains by Eq. (16).

$$M_{total} = \frac{EI}{D}\sqrt{(\varepsilon_E - \varepsilon_W)^2 + (\varepsilon_S - \varepsilon_N)^2} \tag{16}$$

where M_{total} and ε_i are the moments and strains at corresponding direction, EI is the bending stiffness of 3.8E10 N m^2, and D is the inner diameter of tower section at the measurement height of 3.2 m.

The main shaft moment and torque arm motion are measured to validate the proposed 3D DTS model. As the axial and radial forces of the bearings cannot be measured directly, the three components of shaft moments are measured by battery-powered strain gauges attached to the rotating main shaft as shown in Fig. 10. The azimuth angle of the main shaft is measured simultaneously with the strain [39]. The shaft bending moments in the non-rotational coordinate system can be transformed from the rotational coordinate system by Eq. (17).

$$M_{ZN} = M_{ZR}cos\varphi - M_{YR}sin\varphi$$

$$M_{YN} = M_{ZR}sin\varphi + M_{YR}cos\varphi \tag{17}$$

where M_{ZN} and M_{YN} are the yaw and tilt moments of the non-rotational coordinate, M_{ZR} and M_{YR} are the yaw and tilt moments in the rotational coordinate, and φ is the azimuth angle.

To investigate the behavior of the torque arms, the displacements of the torque arm on both the port and starboard sides are measured in the longitudinal (X), horizontal (Y), and vertical (Z) directions by the displacement sensors as shown in Fig. 11 (a) and Fig. 11 (b). The measured displacements indicate the movement of the gearbox relative to the nacelle bedplate since the torque arms link the gearbox to the nacelle bedplate through rubber bushings as shown in Fig. 11 (c) and Fig. 11 (d).

As discussed in the previous section, contamination and internal clearance have a significant effect on the fatigue life of main bearings. Investigations of main bearings regarding these two parameters are carried out on several main bearings at Tomamae Wind Farm in March-April 2014 and December 2015. Contaminations are evaluated by measuring the concentration of the iron particle in the grease lubricant leaking from the bearing as shown in Fig. 12 (a). Internal clearances are measured vertically at the top of the bearing as shown in Fig. 12 (b).

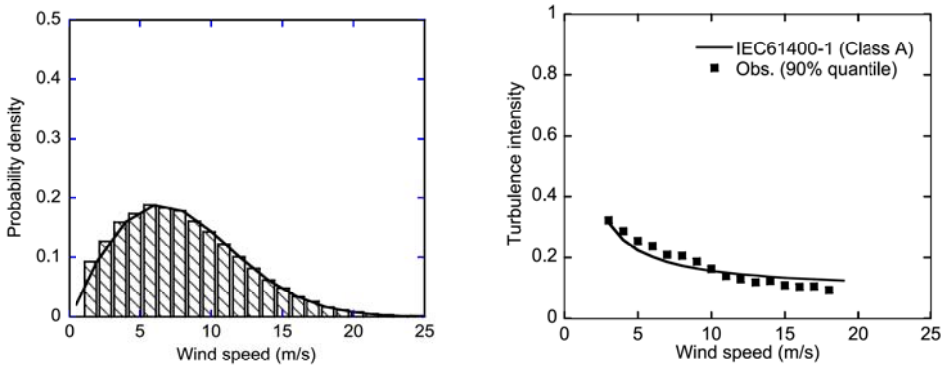

(a) Probability density of wind speed

(b) Turbulence intensity

Fig. 8. Observed wind speed and turbulence intensity.

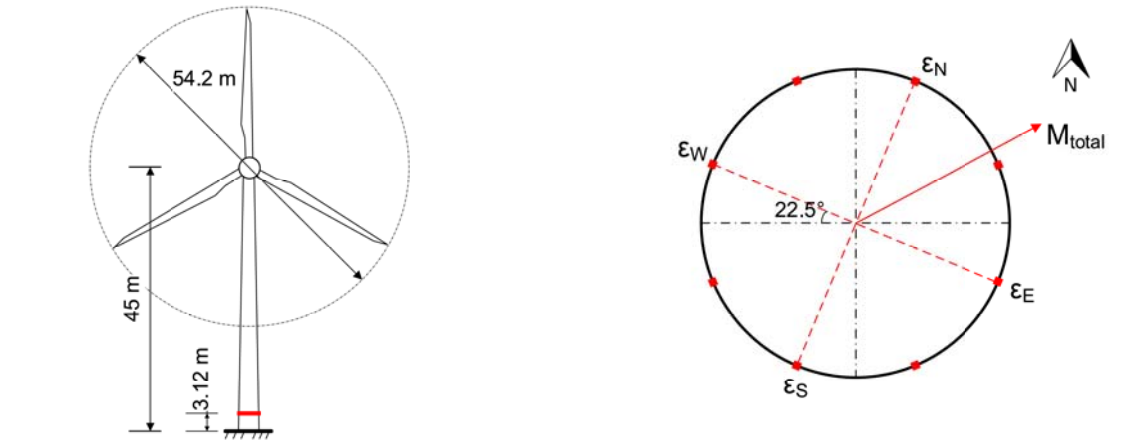

(a) No.3 wind turbine at Tomamae wind farm (b) Layout of strain gauges on the tower shell

Fig. 9. Measurement of tower base bending moments.

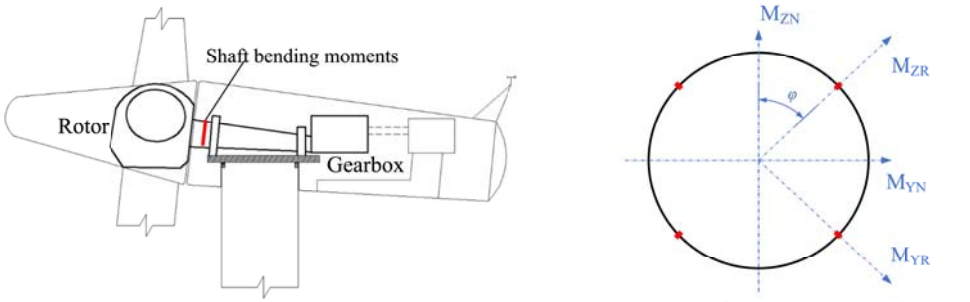

(a) DTS of No.3 wind turbine (b) Layout of strain gauges on the shaft

Fig. 10. Measurement of shaft bending moments.

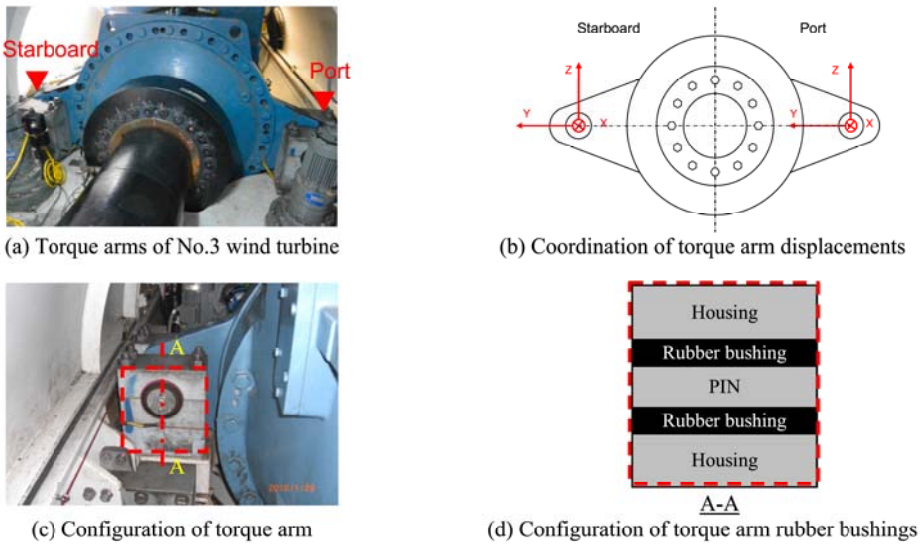

(a) Torque arms of No.3 wind turbine (b) Coordination of torque arm displacements

(c) Configuration of torque arm (d) Configuration of torque arm rubber bushings

Fig. 11. Configuration of torque arm and torque arm rubber bushings.

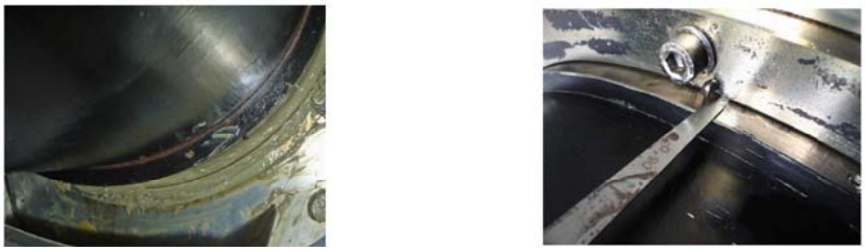

(a) Contamination in the grease lubricant (b) Internal clearance

Fig. 12. Measurement of contamination and internal clearance of main bearing.

3.2. Validation of wind turbine and drivetrain model

The control parameters of aeroelastic model are determined from the measurement in this study. Initial pitch angles α_1 is identified for each wind speed from the predicted power output using a stall control algorithm. The offset angles of three blades in the split pitch control algorithm $\Delta\alpha_2$ are then identified from the power spectra density of the tower base moment as shown in Fig. 13. The tower vibrations are significantly overestimated without split pitch control. Spruce and Turner [14] pointed out that the split pitch control algorithm is an effective method to suppress tower vibrations due to negative damping. This algorithm uses different offset angles for three blades. One blade has no offset, and the other two blades have the opposite offset. Split pitch control suppresses tower vibration by increasing the offset angles, gradually approaching the observed value. Offset angles are determined for each wind speed of 16, 18 and 20 m/s. Furthermore, a pitch angle imbalance $\Delta\alpha_3$ of $\pm$ 0.3 degree is considered according to GL 2010 [29]. The identified total pitch angles for all blades are summarized in Table 9.

The power curve and rotational speed predicted by the proposed aeroelastic wind turbine model using the identified parameters show good agreements with the measured values as shown in Fig. 14. This indicates that the proposed aeroelastic model can favorably predict the torque acting on the main shaft. The predicted average and standard deviation of the tower base moments also agree well with the measured values as shown in Fig. 15, indicating that the proposed aeroelastic model can capture the rotor thrusts well. The predicted standard deviations for wind speeds above 16 m/s without split pitch control are very large due to the negative aerodynamic damping in high wind speed region [13], while when the split pitch control is used, those agree well with the measured values.

For the 3D DTS model, the stiffnesses of torque arm k_{ty} and k_{tz} in the Y and Z directions are determined by the average moments and 3D torque arm displacements and are calculated using Eqs. (18) and (19).

$$k_{ty} = \frac{F_{ty}}{2\Delta_y} = \frac{F_{by}}{2\Delta_y} = \frac{M_z}{2L_1\Delta_y} \tag{18}$$

$$k_{tz} = \frac{F_{tz}}{2\Delta_z} = \left(-F_{zD} + \frac{M_x}{L_5}\right)/(2\Delta_z) = \left(-\frac{M_y}{L_1} + \frac{M_x}{L_5}\right)/(2\Delta_z) \tag{19}$$

where F_{ty} and F_{tz} are the lateral and vertical forces on the torque arm, F_{by} and F_{bz} are the lateral and vertical forces on the downwind side of the main bearing, which balance with M_z and M_y, respectively. M_y and M_z are the moments acting on the hub, Δ_x, Δ_y and Δ_z are the torque arm displacements in X, Y and Z directions as shown in Fig. 19, L_1 and L_5 are shown in Fig. 2 and defined in Table 4. Fig. 16 shows the observed torque arm displacements and forces on the torque arm in the Y and Z directions. The observed nonlinear stiffness shows a similar trend obtained from Keller et al. [34].

The stiffness k_{tx} used in the proposed 3D DTS model is estimated using the determined k_{ty} and k_{tz} and the measured torque arm displacement in X direction, since the thrust force is mainly exerted by the main bearing. The displacement of the port side torque arm in the X direction ranges between the displacements in Y and Z directions, while the displacement of the starboard side torque arm is

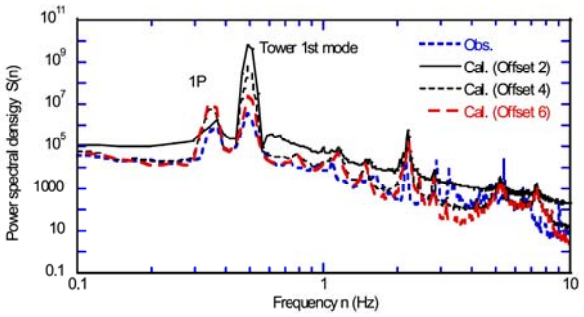

Fig. 13. Power spectral densigy of tower base moments with different offset angles for the split pitch control.

Table 9
Summary of pitch angles and rotor imbalance used in the aeroelastic wind turbine model.

Speed(m/s)	α_1(Initial pitch angle)			$\Delta\alpha_2$(Offset pitch angle)			$\Delta\alpha_3$(Pitch imbalance)			Total pitch angle (α)		
	Blade1	Blade2	Blade 3	Blade1	Blade2	Blade3	Blade1	Blade2	Blade3	Blade1	Blade2	Blade 3
6	0	0	0	0	0	0	−0.3	0	0.3	−0.3	0	0.3
8	0	0	0	0	0	0	−0.3	0	0.3	−0.3	0	0.3
10	0	0	0	0	0	0	−0.3	0	0.3	−0.3	0	0.3
12	0	0	0	0	0	0	−0.3	0	0.3	−0.3	0	0.3
14	−1.22	−1.22	−1.22	0	0	0	−0.3	0	0.3	−1.52	−1.22	−0.92
16	−1.75	−1.75	−1.75	−1	0	1	−0.3	0	0.3	−3.05	−1.75	−0.45
18	−0.94	−0.94	−0.94	−4	0	4	−0.3	0	0.3	−5.24	−0.94	3.36
20	−0.04	−0.04	−0.04	−6	0	6	−0.3	0	0.3	−6.34	−0.04	6.26

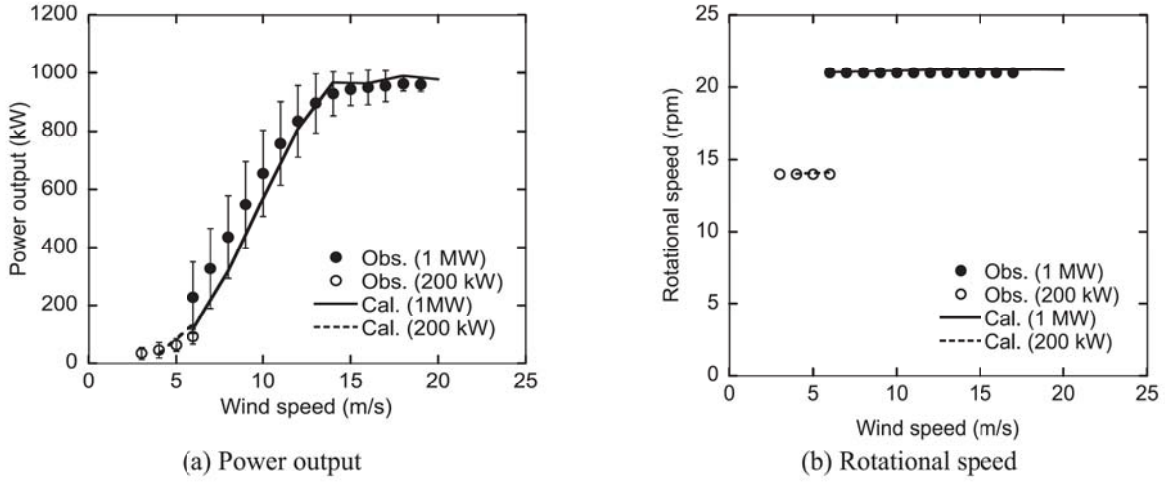

Fig. 14. Comparison between predicted and observed power out and rotational speed of wind turbine.

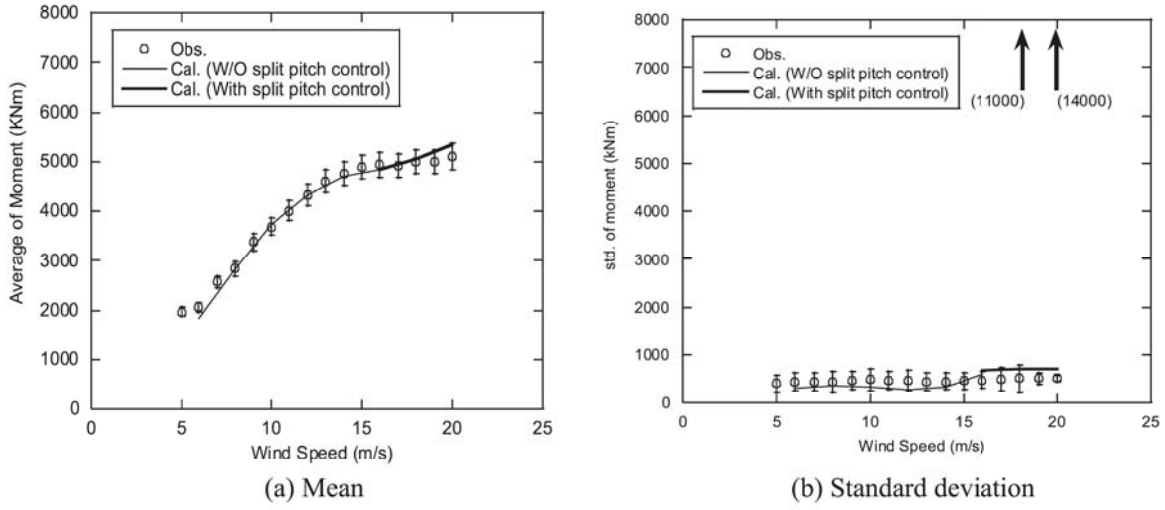

Fig. 15. Variation of measured and predicted tower base moment with mean wind speeds.

close to 0. Hence, the proposed 3D DTS model is used to identify the stiffness in X direction according to the measured displacement in the X direction under the assumption that rubber bushing is isotropic in three directions.

To simplify the simulation of the torque arm, a trilinear model is applied in each direction. The identified k_{tx}, k_{ty} and k_{tz} are summarized in Table 10. The predicted relationships between displacements and forces in the X, Y and Z directions are shown in Fig. 16 and compared with the measurements.

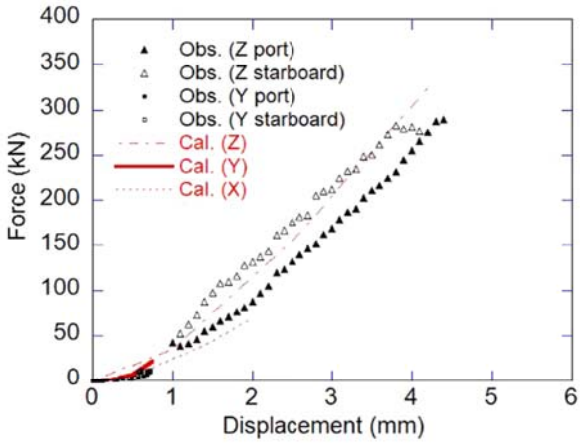

Fig. 16. Relationship between force and displacement of torque arm.

Table 10
Identified torque arm stiffness in the X, Y and Z directions.

Notation	Stiffness (kN mm^{-1})	Displacement (mm)	Force (kN)
k_{tx}	20	0–0.75	0–15
	40	0.75–1.4	15–40
	50	1.4–2	40–70
k_{ty}	8	0–0.25	0–2
	22	0.25–0.5	2–5
	60	0.5–0.75	7.5—25
k_{tz}	60	0.75–1	25—40
	80	1–2.5	40–155
	100	2.5–4.2	155—325

Rubber bushings are provided as a damping function for the torque arm to isolate vibration and noise isolation. Neto and Santos [40] concluded that the damping ratio of natural rubber is approximately 7.5 %, which is taken as the modal damping ratio of the proposed 3D DTS model in this study.

The radial and axial stiffnesses of spherical roller bearings are calculated by applying initial loads in Z and X directions due to the gravity and tilt angle of rotor, main shaft and gearbox. The equivalent radial and axial linear stiffness of the main bearing are estimated using the empirical formulas by Gargiulio [41] as follows:

$$\delta_r = 0.10778 \frac{(F_r/iZ)^{3/4}}{l_{we}^{1/2}\cos\alpha^{7/4}} \tag{20}$$

$$\delta_a = 0.03218 \frac{(F_a/iZ)^{3/4}}{l_{we}^{1/2}\cos\alpha^{7/4}} \tag{21}$$

where i is the number of rows, Z is the number of rolling elements in each row, l_{we} is the effective roller length and α is the nominal contact angle, whose values are shown in Table 6. The radial load F_r and axial load F_a are calculated using 1D DTS model considering the gravity and tilt angle of rotor, main shaft and gearbox, whose values are shown in Table 2 and Table 4. Note that the coefficients in Eqs. (20) and (21) are converted because the units have changed from lbf and inches to N and mm. Table 11 lists the calculated bearing stiffness in the radial and axial directions.

For wind turbines, the rotor and main shaft gravities are mainly supported by the main bearing, the bearing stiffness in Z direction is the same as the radial stiffness of the main bearing. The bearing load in the Y direction is much smaller than that in the Z direction and the positive clearance is observed in the measured main bearing. Therefore, the bearing stiffness in the Y direction is assumed to be proportional to the axial stiffness of the main bearing and is identified to reproduce the measured torque arm displacement in the Y direction. The bearing stiffness in the X direction is affected by the connected gearbox and the actual bearing stiffness in the X direction is assumeed to be propotional to the axial stiffness of the main bearing and is identified to reproduce the measured torque arm displacement in the X direction. Table 12 summarizes the idetified bearing stiffnesses in the X, Y and Z directions.

The shaft torque and bending moments are predicted by the 3D DTS model described in section 2.2 using the identified parameters. The predicted average values and standard deviations of shaft torque and bending moments by the conventional 1D DTS model and the proposed 3D DTS model are shown in Fig. 17 and compared with the measured values. The mean torque M_x is found to be dominant

Table 11
Calculated bearing stiffness in the radial and axial directions.

Notation	Initial load (kN)	Initial deformation (mm)	Stiffness (kN mm^{-1})
k_a	32	0.0698	229
k_r	440	0.0589	3734

Table 12
Idetified bearing stiffness in the X, Y and Z directions.

Notation	Idetified bearing stiffness (kN mm^{-1})	Values of stiffness (kN mm^{-1})
k_{bx}	ak_a, $a = 0.44$	100
k_{by}	bk_a, $b = 0.66$	150
k_{bz}	ck_r, $c = 1$	3734

among all components, and the predicted values by the1D and 3D models show good agreement with the measured values. This indicates that the 1D model can be to estimate the mean shaft torque. The variations in shaft tilt bending moment M_{yN} and yaw bending moment M_{zN} in the non-rotational coordinate are slightly overestimated by the 1D model as shown in Fig. 17 (d) and Fig. 17 (f). Guntur et al. [16] also pointed out that these overestimations were due to the neglect of damping effects by using DTS model in the FAST [10]. By applying the 3D model that considers the damping effect of DTS, the overestimation of the 1D model is improved.

The mean and standard deviation of torque arm displacement predicted by the 1D and 3D DTS models are shown in Fig. 18. The maximum mean displacements in the X, Y and Z directions are approximately 2 mm, 1 mm, and 3.5 mm, respectively. The displacement in the Z direction is dominant and symmetric on the starboard and port sides since the torque Mx is dominant. The displacement in the Y direction is minimal and exhibits the same movement on both sides since the yaw moment M_z is much smaller than the torque M_x. The displacements in the X direction are asymmetric if the starboard is large and the port movement is small because the torque arms are affected by both the yaw moment M_z and thrust force F_x. The yaw moment M_z causes the port side to move upwind and the starboard side to move downwind. Meanwhile, the thrust force F_x is not completely taken by the main bearing and partially acts on the torque arms causing a downwind motion on both sides. As a result, the starboard side movement is superimposed, while the port side movement is canceled out. Fig. 19 illustrates an overview of three-dimensional torque arm movements, where Δ_{ys} and Δ_{yp} are the same as Δ_y, the absolute value of Δ_{zs} and Δ_{zp} are the same as Δ_z. It is found that the maximum standard deviation of displacements in the X, Y and Z directions are approximately 0.2 mm, 0.15 mm, and 0.35 mm. This indicates that the standard deviations are about one-tenth of the mean values.

Since the motion of the torque arm cannot be predicted by the 1D model, all displacements of the torque arm predicted by the 1D model are zero. The mean and standard deviation of torque arm displacement predicted by the 3D model considering two elastic torque arms show good agreement with the measured values.

3.3. *Fatigue prediction of main bearing*

Parameters of pounding model of main bearing are evaluated. At the normal operating stage with internal clearance, the roller stiffness is converted into the initial bearing stiffness k_b and the pounding stiffness k_p as described in Fig. 3 (b). The pounding stiffness k_p of 150 kN/mm in Table 13 is set to the same value as the bearing stiffness k_{by} without pounding because it is assumed that the pounding occurs due to shaft movement in the Y direction. The ratio of k_b with pounding to k_b without pounding is set to 0.1 based on Nakamura et al. [42]. The normal internal clearance at the top of main bearing in the vertical direction Z is decided by a clearance as shown in ISO 5753 [43]. The maximum value of normal clearance is 0.44 mm, and the intermediate value of 0.22 mm is used to evaluate the load factor in this study. Considering geometrical relationship of main bearing, the clearance in the horizontal direction Y is estimated to be about 1/2 of the vertical clearance [44]. The parameters of pounding model are summarized in Table 13.

According to the motion analysis of the torque arm, the DTS motion in the horizontal direction Y of starboard and port sides is the same, while the motions of those in other directions are different. To clarify the effect of main shaft movement on the main bearing, the effect of pounding on the main bearing is evaluated only in the horizontal direction Y. The stiffness of torque arm is considered as linear to simplify the pounding simulation. The linear stiffness of torque arm is determined by the measured displacement and the corresponding stiffness.

The pounding force is predicted by the pounding model introduced in section 2.3 with the identified parameters. The fluctuating wind loading is simulated using the fluctuating wind speed based on the normal turbulence model as shown in IE61400-1 [28] and the energy loss is considered using the damping ratio in the dynamic analysis. An example of timeseries of predicted bearing loads with and without pounding at a wind speed of 8 m/s is shown in Fig. 20. It is found that the pounding forces fluctuate greatly due to the collision between the roller and the ring. Six turbulence seeds are used for each wind speed to account for simulation uncertainties.

The load factor f_w is obtained from Eq. (11). The variation of predicted load factors with mean wind speeds is shown in Fig. 21. Plots and bars mean the average and standard deviation of the load factors of six seeds respectively. It is found that the predicted load factors

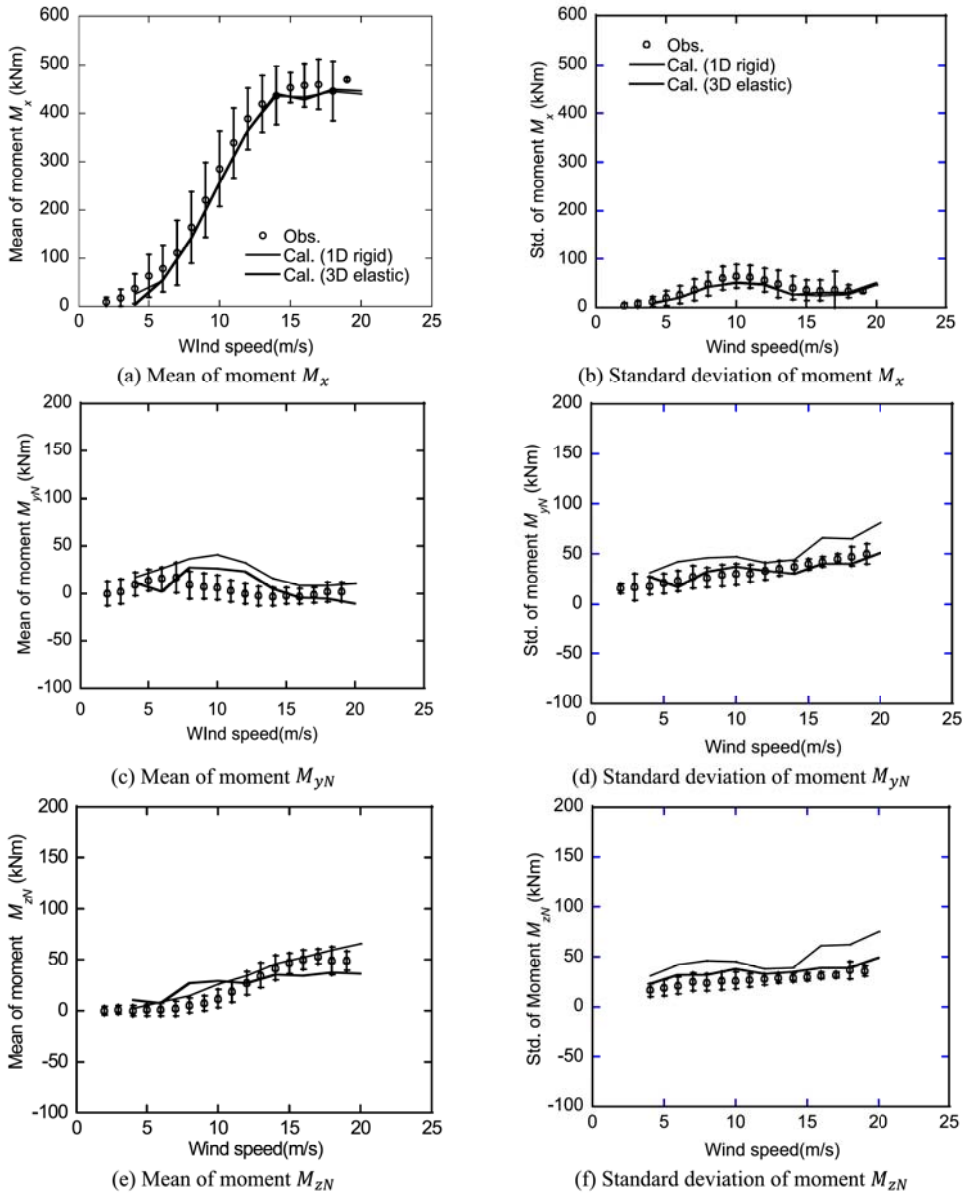

Fig. 17. Variation of predicted and measured shaft moments with mean wind speeds.

range from 1.1 to 1.5, which are comparable to the empirical load factors of 1.2 to 1.5 for the slight pounding category used in the current bearing industry [22]. The equivalent load factor is calculated as 1.3 and used to predict the fatigue life of the bearing.

The contamination and internal clearance parameters are evaluated based on the survey described in section 3.1. The observed contamination and internal clearance of main bearing are plotted in Fig. 22. Contamination of main bearing varies greatly depending on bearing wear during different operating stages. This is because bearing wear causes iron particles from rollers and rings to get into grease lubricant.

This life reduction is reflected by the contamination-related corrected factors a_{ISO} in ISO 281 as shown in Eq. (9). Under normal operating conditions, the contamination is rated in the slight to typical category, because bearings are assembled with moderate sealing capacity and regularly regreased according to maintenance schedules. Practical maintenance criteria in wind farms set the iron particle contamination in bearings to be less than 0.4 wt% [21] under normal operating conditions. ISO 5753 states that the maximum internal clearance within this criterion is 0.44 mm. This is the areas where the iron particle contamination is 0.4 wt% or less and the internal clearance is 0.44 mm or less as shown by green areas in Fig. 22. Therefore, the maximum value of 0.44 mm is used as the normal internal clearance to predict the life ratio a_ε. From Fig. 5, the life ratio a_ε is calculated to be 0.276. which is used to predict the fatigue life of bearing.

To investigate the mechanism of main bearing lifetime shorting, the rating life L_{10} is predicted for each case as listed in Table 14.

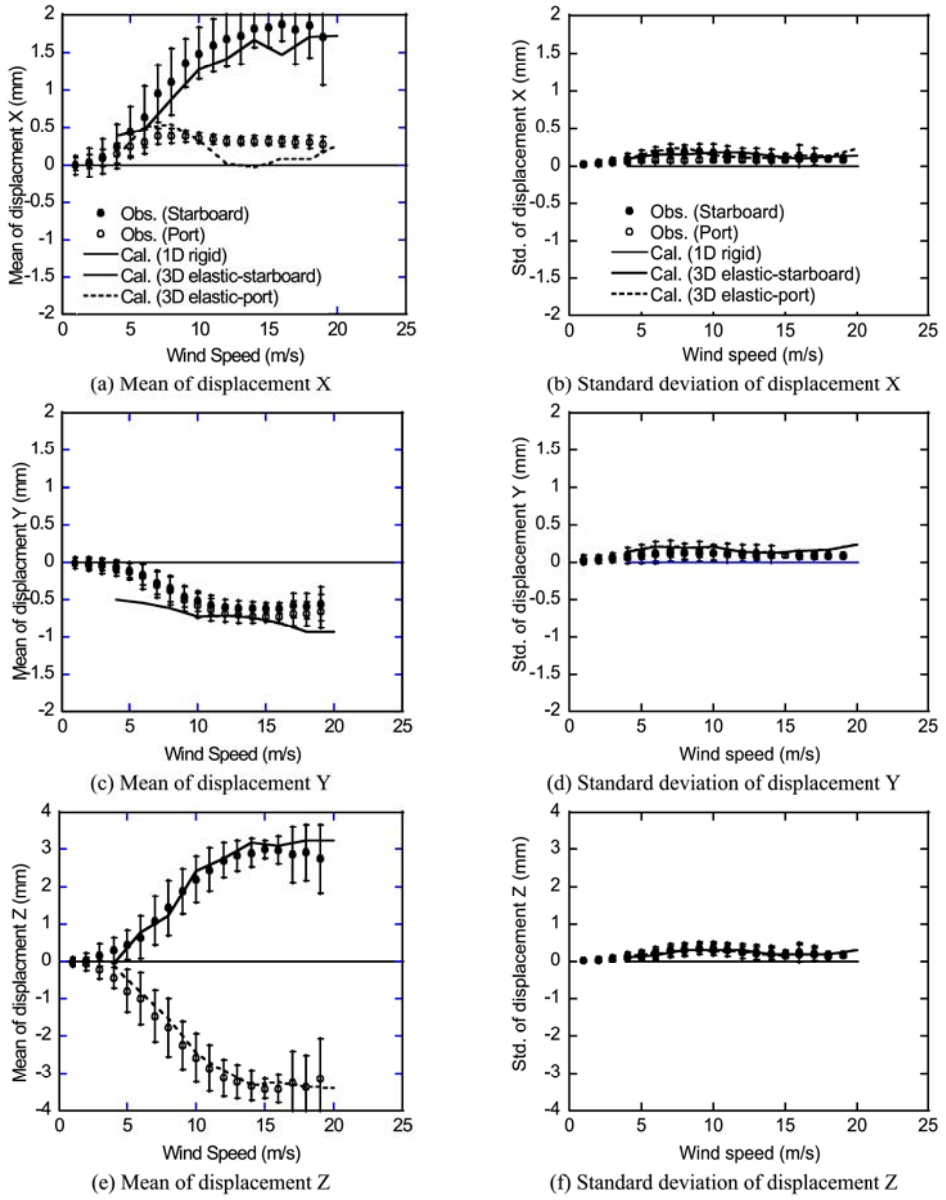

Fig. 18. Variation of measured and predicted torque arm motions with mean wind speeds,

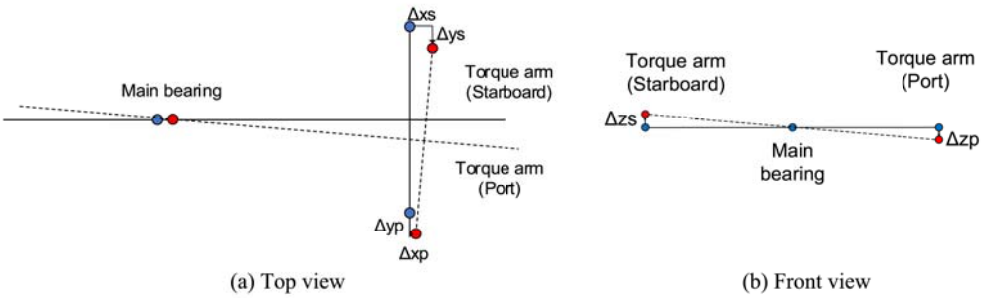

Fig. 19. Summary of analyzed torque arm motions in three directions, where blue circles represent the original location of DTS supports, and red circles indicate the support locations with displacements.

Table 13
Identified parameters used in the main bearing pounding model.

Notation	Unit	W/O pounding	With pounding
k_b	kN/mm	150	15
k_p	kN/mm	0	150
d	mm	0	0.11

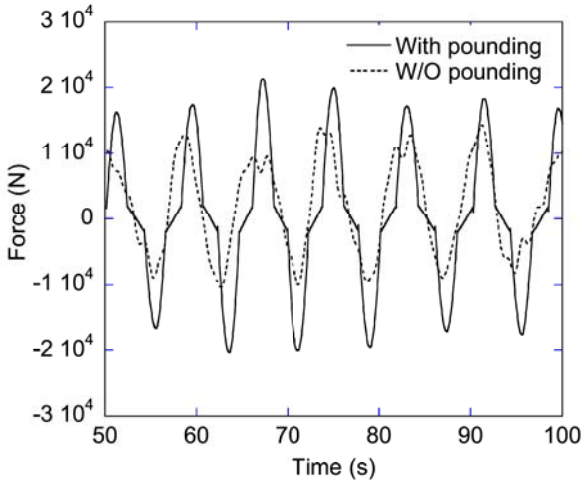

Fig. 20. Predicted bearing forces with and without pounding.

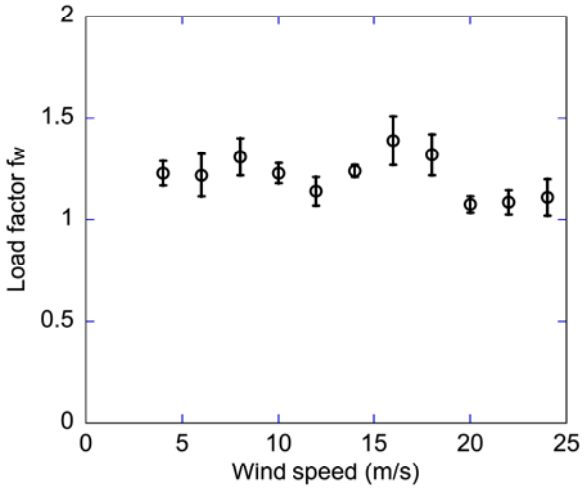

Fig. 21. Variation of load factor with mean wind speeds.

Considering the probability of occurrence of wind speed as a weight, the equivalent rating life L_{10equ} can be evaluated as shown in Eq. (22), using a cumulative damage model based on Miner's rule [29].

$$L_{10equ} = \frac{\sum q_i}{\sum \frac{q_i}{L_{10i}}} \tag{22}$$

where q_i is the occurrence probability and L_{10i} are the rating life at the wind speed i.

The observed rating life L_{10} of the Tomamae Wind Farm is derived from the onsite damage records of main bearings from 1999 to 2017. The time from the start of operation to the first repair is considered as the lifetime as shown in Fig. 23 (a). Since some operations of main bearing were interrupted due to unexpected accidents or unscheduled maintenance, a censoring method is applied to these abnormal fatigue data [45]. Based on the experimental and numerical studies on the rolling fatigue [46,47], it is known that the fatigue

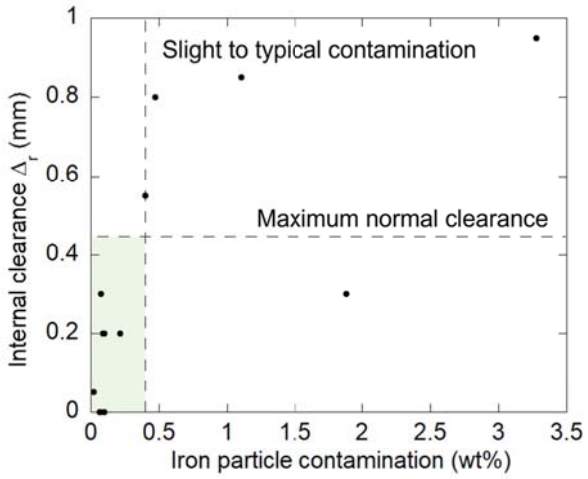

Fig. 22. Observed contamination and internal clearance of main bearings.

Table 14
Cases of rating life L_{10} prediction.

Case	ISO original	ISO with a_e	ISO with a_e and f_w
a_e	1	0.276	0.276
f_w	1	1	1.3
a_{ISO}		Slight to typical contamination	

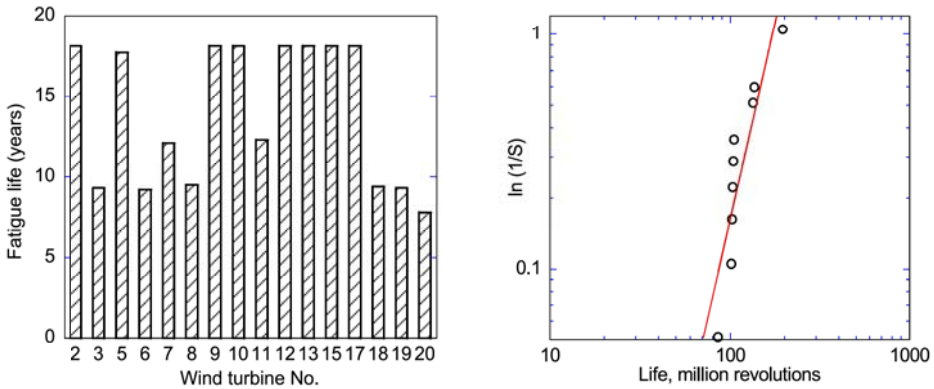

(a) Fatigue life records (b) Weibull distribution of fatigue life

Fig. 23. Observed rating life of main bearings in Tomamae Wind Farm.

life of bearings follows a Weibull distribution as expressed in Eq. (23). In this study, the accumulative failure rates are obtained from damage records of main bearing, and the relationship between reliability and life is shown in Fig. 23 (b). Finally, the observed main bearing rating life L_{10} is calculated to be 9 years with reliability S of 90 %.

$$ln\frac{1}{S} = AL_s^e \tag{23}$$

where S is the reliability, A is a constant as the material factor, L_s is the service life and e is the Weibull slope.

Fig. 24 shows the results of comparing the predicted rating life L_{10} with the observed value for each case as listed in Table 14. The predicted rating life L_{10} considering both parameters is 9.7 years and favorably agrees with the recorded value of 9 years, while the original formula in ISO 281 overestimates the rating life by about 14.5 times. The rating life is reduced by a factor of 3.6 and 4.0 due to the influence of the life ratio a_e and the load factor f_w.

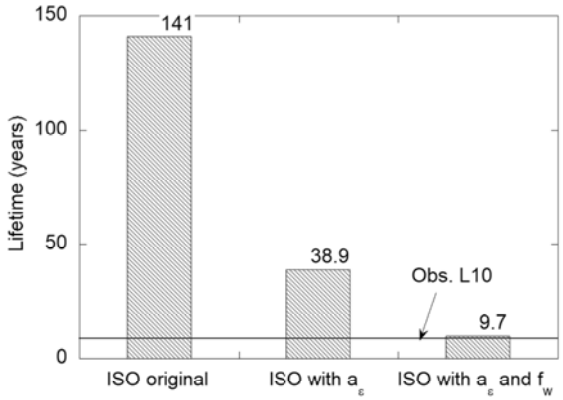

Fig. 24. Observed and predicted rating life L_{10} with different parameters.

4. Conclusion

In this study, the fatigue prediction of wind turbine main bearing is performed by numerical models and field measurements in consideration of internal clearances and pounding forces. 3D DTS model is proposed for wind turbines with TPM configuration. The load factors are evaluated by a pounding model of main bearing. The formulas in ISO 281 to predict the bearing rating life L_{10} are modified by introducing two new parameters: life ratio and load factor. The following conclusions are obtained:

1) 3D DTS model is proposed to predict the displacements of the drivetrain system in the X, Y and Z directions. The predicted shaft moments and torque arm motions by the proposed 3D DTS model for TPM match well with the measurements, while the conventional 1D DTS model overestimates the shaft bending moments and cannot capture the torque arm motions. The maximum mean displacements in the X, Y and Z directions are approximately 2.0 mm, 1.0 mm, and 3.5 mm, respectively. Since the torque M_X is dominant, the displacements in the Z direction are dominant and symmetrical on the starboard and port sides.
2) The load factor is proposed to predict the main bearing fatigue life and evaluated by the numerical simulation considering the main bearing pounding. The predicted load factors range from 1.1 to 1.5 with an equivalent value of 1.3, which corresponds to the empirical load factors of 1.2 to 1.5 used in the current bearing industry for slight pounding category.
3) The two parameters of life ratio a_ε and load factor f_w are applied to predict the main bearing fatigue life. The predicted rating life L_{10} considering both parameters favorably agrees with the recorded value, and the rating life is reduced by a factor of 3.6 and 4.0 due to the influence of the life ratio a_ε and the load factor f_w, respectively. On the other hand, the original formula in ISO 281 significantly overestimates the rating life by about 14.5 times.

CRediT authorship contribution statement

Takeshi Ishihara: Writing – review & editing, Supervision, Project administration, Methodology, Funding acquisition, Conceptualization. **Shuai Wang:** Writing – original draft, Visualization, Validation, Software, Methodology, Investigation, Data curation. **Yuka Kikuchi:** Writing – review & editing, Visualization, Resources, Methodology, Data curation.

Declaration of competing interest

The authors declare that they have no known competing financial interests or personal relationships that could have appeared to influence the work reported in this paper.

Acknowledgement

This research is carried out as a part of research and development of smart maintenance project supported by the New Energy and Industrial Technology Development Organization (NEDO). The authors wish to express their deepest gratitude to the concerned parties for their assistance.

Data availability

The authors do not have permission to share data.

References

[1] D. McMillan, G.W. Ault, Condition monitoring benefit for onshore wind turbines: sensitivity to operational parameters, IET Renew. Power Gener. 2 (1) (2008) 60–72, https://doi.org/10.1049/iet-rpg:20070064.
[2] J. Helsen, F. Vanhollebeke, D. Vandepitte, W. Desmet, Some trends and challenges in wind turbine upscaling, Int. Conf. Noise Vib. Eng. 2012, ISMA 2012, Incl. USD 2012 Int. Conf. Uncertain. Struct. Dyn. 6 (2012) 4345–4359.
[3] Y. Guo, T. Parsons, K. Dykes, R.N. King, A systems engineering analysis of three-point and four-point wind turbine drivetrain configurations, Wind Energy 20 (3) (2017) 537–550, https://doi.org/10.1002/we.2022.
[4] D. Brake, WTG SRB Main Bearing Failures, presented at the 2013 UVIG wind turbine/plant operations & maintenance users group meeting, 2013.
[5] Eurus Energy Holdings Corporation, Report on accident of Tomamae Green Hills Wind Park No.11 WTG., 2014. (in Japanese).
[6] Z. Jiang, X. Huang, H. Liu, et al., Dynamic reliability analysis of main shaft bearings in wind turbines, Int. J. Mech. Sci. 235 (2022) 107721, https://doi.org/10.1016/j.ijmecsci.2022.107721.
[7] W. Zhao, Z. Jiang, P. Zhang, X. Huang, Reliability Sensitivity Analysis of Main Shaft Bearings of Wind Turbines Subject to Subsurface Stress, Machines 11 (7) (2023) 681, https://doi.org/10.3390/machines11070681.
[8] L. Campoverde-Vilela, M.C. Feijoo, Y. Vidal, J. Sampietro, C. Tutiven, Anomaly-based fault detection in wind turbine main bearings, Wind Energy Sic. 8 (2023) 557–574, https://doi.org/10.5194/wes-8-557-2023.
[9] R.M. Arias Velasquez, Bearings faults and limits in wind turbine generators, Results Eng. 21 (2024) 101891, https://doi.org/10.1016/j.rineng.2024.101891.
[10] J. Kenworthy, E. Hart, J. Stirling, A. Stock, J. Keller, Y. Guo, J. Brasseur, R. Evans, Wind turbine main bearing rating lives as determined by IEC 61400–1 and ISO 281: A critical review and exploratory case study, Wind Energy 27 (2) (2024) 179–197, https://doi.org/10.1002/we.2883.
[11] A. Yamaguchi, P.W. Sarli, T. Ishihara, Extreme load estimation of the wind turbine tower during power production, Wind Eng. 45 (2021) 93–106, https://doi.org/10.1177/0309524X19872766.
[12] A. Yamaguchi, I. Yousefi, T. Ishihara, Reduction in the fluctuating load on wind turbines by using a combined nacelle acceleration feedback and lidar-based feedforward control, Energies 13 (2020), https://doi.org/10.3390/en13174558.
[13] J.M. Jonkman, Influence of control on the pitch damping of a floating wind turbine, 46th AIAA Aerosp, Sci. Meet. Exhib. (2008), https://doi.org/10.2514/6.2008-1306.
[14] C.J. Spruce, J.K. Turner, Tower vibration control of active stall wind turbines, IEEE Trans. Control Syst. Technol. 21 (4) (2013) 1049–1066, https://doi.org/10.1109/TCST.2013.2261298.
[15] J.M. Jonkman, M.L. Buhl, FAST User's Guide, National Renewable Energy Laboratory Technical Report NREL/TP-500-38230, 2005.
[16] S. Guntur, J. Jonkman, R. Sievers, M.A. Sprague, S. Schreck, Q. Wang, A validation and code-to-code verification of FAST for a megawatt-scale wind turbine with aeroelastically tailored blades, Wind Energy Sci. 2 (2017) 443–468, https://doi.org/10.5194/wes-2-443-2017.
[17] E.A. Bossanyi, G.H. Bladed, User Manual, Garrad Hassan Bladed (2009).
[18] E. Hart, B. Clarke, G. Nicholas, A.K. Amiri, J. Stirling, J. Carroll, R. Dwyer-Joyce, A. McDonald, H. Long, A review of wind turbine main bearings design, operation, modelling, damage mechanisms and fault detection, Wind Energ Sci. 5 (1) (2020) 105–124, https://doi.org/10.5194/wes-5-105-2020.
[19] M. Cardaun, B. Roscher, R. Schelenz, G. Jacobs, Analysis of wind-turbine main bearing loads due to constant yaw misalignments over a 20 years timespan, Energies 12 (9) (2019) 1768, https://doi.org/10.3390/en12091768.
[20] K. Shoda, Y. Yatomi, K. Iwasaki, K. Karikomi, H. Takeuchi, T. Yoshinaga, Study on reliability improvement of gear box for wind turbine (1st Report, Failure Mechanism of Bearing by Rotor Moment), Trans. Jpn. Soc. Mech. Eng. Ser. C. 79 (806) (2013) 3904–3919, https://doi.org/10.1299/kikaic.79.3904 (in Japanese).
[21] NEDO, Report on smart maintanence technology development (fatigue prediction), New Energy and Industrial Technology Development Organization, 2019.
[22] NTN Corporation, Ball and Roller bearings CAT. NO. 2203-3/E., Osaka, 2024. https://www.ntnglobal.com/en/products/catalog/pdf/2203E.pdf.
[23] S. Nagarajaiah, X. Sun, Base-isolated FCC building: impact response in Northridge earthquake, J. Struct. Eng. 127 (9) (2001) 1063–1075, https://doi.org/10.1061/(ASCE)0733-9445(2001)127:9(1063).
[24] B.F. Maison, K. Kasai, Analysis for type of structural pounding, J. Struct. Eng. 116 (4) (1990) 957–977, https://doi.org/10.1061/(ASCE)0733-9445(1990)116:4(957).
[25] P. Zhu, M. Abe, Y. Fujino, Evaluation of pounding countermeasures and serviceability of elevated bridges during seismic excitation using 3D modeling, Earthquake Engng. Struct. Dyn. 33 (5) (2004) 591–609, https://doi.org/10.1002/eqe.365.
[26] K. Kawashima, An analytical model of contact and impact in dynamic response analysis, Proc. Japan Soc. Civ. Eng. 1981 (308) (1981) 123–126, https://doi.org/10.2208/jscej1969.1981.308_123 (In Japanese).
[27] T. Takeda, T. Mizutani, T. Nagayama, Y. Fujino, Reproduction of cable-stayed bridge seismic responses involving tower–girder pounding and damage process estimation for large earthquakes, J. Bridge Eng. 24 (2) (2019) 04018112, https://doi.org/10.1061/(ASCE)BE.1943-5592.0001336.
[28] IEC 61400-1, Wind energy generation systems-part 1: Design requirements, fourth edition, International Electrotechnical Commission, Switzerland, 2019.
[29] GL2010, Rules and guidelines industrial services: guideline for the certification of offshore wind turbines, Germanischer Lloyd, Hamburg, 2010.
[30] Iso, 281, Rolling bearings - dynamic load ratings and rating life, International Organization for Standardization, Switzerland, 2007.
[31] G. Lundberg, A. Palmgren, Dynamic capacity of rolling bearings, Acta. Polytech Mech. Eng. Ser. 1 (3) (1947) 5–50.
[32] J. Halme, P. Andersson, Rolling contact fatigue and wear fundamentals for rolling bearing diagnostics -state of the art P, Inst. Mech. Eng. Pt. J 224 (4) (2010) 377–393, https://doi.org/10.1243/13506501JET656.
[33] T. Ishihara (Ed.), Guidelines for Design of Wind Turbine Supprot Structures and Foundation, Japan Society of Civil Engineers (JSCE), Tokyo, 2010 in Japanese.
[34] Y. Guo, R.G. Parker, Dynamic modeling and analysis of a spur planetary gear involving tooth wedging and bearing clearance nonlinearity, Eur. J. Mech. A/solids 29 (2010) 1022–1033, https://doi.org/10.1016/j.euromechsol.2010.05.001.
[35] J. Keller, Y. Guo, L. Sethuraman, J. Keller, Y. Guo, L. Sethuraman, Gearbox reliability collaborative investigation of gearbox motion and high-speed-shaft loads, Nrel/tp-5000-65321 (2016).
[36] F.B. Oswald, E.V. Zaretsky, J.V. Poplawski, Effect of internal clearance on load distribution and life of radially loaded ball and roller Bearing. NASA/TM—2012-217115, National Aeronautics and Space Administration (2012). https://ntrs.nasa.gov/api/citations/20120008398/downloads/20120008398.pdf.
[37] NSK Ltd., Bearings, Technical Report, CAT. No. E728g, Tokyo, 2013. https://www.nsk.com/content/dam/nsk/common/catalogs/ctrgPdf/bearings/e728g.pdf.
[38] G.W. Qian, T. Ishihara, Numerical study of wind turbine wakes over escarpments by a modified delayed detached eddy simulation, J. Wind Eng. Ind. Aerodyn. 191 (2019) 41–53, https://doi.org/10.1016/j.jweia.2019.05.004.
[39] S. Oh, Field measurement of the main shaft dynamic loadings on a fixed-speed active stall controlled 1mw wind turbine, First Int. Symp. Flutter Its Appl. (2016) 697–704.
[40] F.P.L. Neto, M.B. Dos Santos, A procedure for the parametric identification of viscoelastic dampers accounting for preload, J. Brazilian Soc. Mech. Sci. Eng. 34 (2012) 213–218, https://doi.org/10.1590/S1678-58782012000200013.
[41] E.P. Gargiulio, A simple way to estimate bearing stiffness, Mach. Des. 52 (17) (1980) 107–110.
[42] M. Nakamura, R. Kawai, I. Moriwaki, Stiffness evaluation of tapered roller bearing using tooth flank film elements, Trans. Jpn. Soc. Mech. Eng. Ser. C. 77 (775) (2011) 604–613, https://doi.org/10.1299/kikaic.77.604 (in Japanese).
[43] ISO 5753-1, Rollering bearings-internal clearance, International Organization for Standardization, Switzerland, 2009.
[44] F.B. Oswald, E.V. Zaretsky, J.V. Poplawski, Interference-fit life factors for roller bearings, Tribol. Trans. 52 (2009) 415–426, https://doi.org/10.1080/10402000802687890.

[45] L.G. Johnson, Statistical treatment of fatigue experiments, first edition, Elsevier Sciense Ltd, 1964. ISBN 978-0444403223.
[46] F. Sadeghi, B. Jalalahmadi, T.S. Slack, N. Raje, N.K. Arakere, A review of rolling contact fatigue, J. Tribol. 131 (2009) 1–15, https://doi.org/10.1115/1.3209132.
[47] T.A. Harris, M.N. Kotzalas, Rolling bearing analysis, fifth edition, CRC Press, 2006.